Electronic Supplementary Material (ESI) for Nanoscale.

Supplementary Information

Deciphering Ion Concentration Polarization-Based Electrokinetic Molecular Concentration at the Micro-Nanofluidic Interface: Theoretical Limits and Scaling Laws

Wei Ouyang,[a,b] Xinghui Ye,[c] Zirui Li,[*c] Jongyoon Han*[a,b,c,d]

[a]*Department of Electrical Engineering and Computer Science, Massachusetts Institute of Technology, Cambridge, Massachusetts, 02139, USA. E-mail: jyhan@mit.edu*

[b]*Research Laboratory of Electronics, Massachusetts Institute of Technology, Cambridge, Massachusetts, 02139, USA*

[c]*Institute of Laser and Optoelectronic Intelligent Manufacturing, College of Mechanical and Electrical Engineering, Wenzhou University, Wenzhou, 325035, P.R. China. E-mail: lizirui@gmail.com*

[d]*Department of Biological Engineering, Massachusetts Institute of Technology, Cambridge, Massachusetts, 02139, USA*

Section 1. Derivation of the EK limit

Because the electrophoretic force is co-directional with the fluid drag force for the cation and counter-directional for the anion and analyte particle, the fluxes of charged species satisfy $J_1^\infty \gg J_2^\infty$, $J_1^\infty \gg J_3^\infty$, as supported by the simulation data in Fig. S1-1.

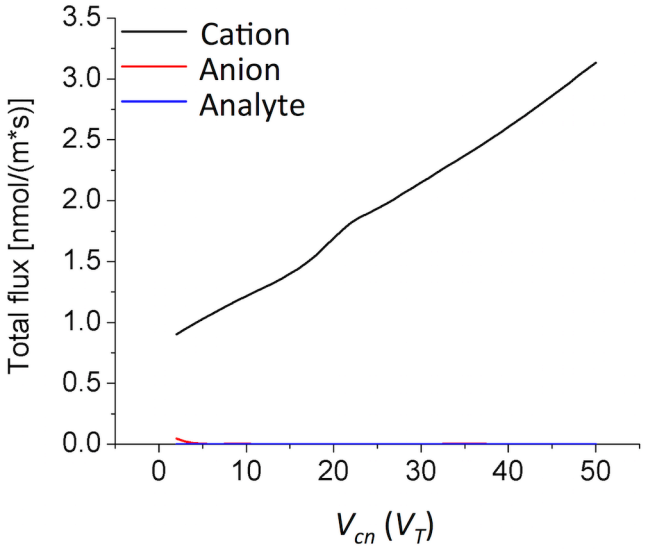

Fig. S1-1. The fluxes of the cation, anion and analyte particle at the steady state at different V_{cn}'s.

In this derivation, we will only consider symmetric binary electrolytes (e.g. KCl) as the buffer, i.e. $D_1 = D_2, Z_1 = -Z_2, C_1^0 = C_2^0$. The electroneutrality is generally obeyed except in the space charges layers in the ion depletion zone, so we can approximate that $C_1^\infty \approx C_2^\infty$ for $x<L/2$. By approximating $J_2^\infty \approx 0$ and $J_3^\infty \approx 0$, the fluxes of the cation, anion, and analyte can be written as,

$$J_1^\infty = -D_1 \frac{dC_1^\infty}{dx} + (\bar{u} + \mu_1 E) C_1^\infty = J_C, \quad \text{S1.1}$$

$$J_2^\infty = -D_2 \frac{dC_2^\infty}{dx} + (\bar{u} - \mu_2 E) C_2^\infty \approx 0, \quad \text{S1.2}$$

$$J_3^\infty = -D_3 \frac{dC_3^\infty}{dx} + (\bar{u} - \mu_3 E) C_3^\infty \approx 0, \quad \text{S1.3}$$

where J_C is constant with respect to x ($x<L/2$) at the steady state, and $\bar{u}$ is independent of x due to the incompressibility of fluid.

Subtracting Eq. S1.2 from Eq. S1.1 yields that,

$$\mu_2 E C_2^\infty \approx J_C / 2. \quad \text{S1.4}$$

Substituting Eq. S1.4 to Eq. S1.2 yields that,

$$-D_2 \frac{dC_2^\infty}{dx} + \bar{u} C_2^\infty - \frac{J_C}{2} \approx 0. \quad \text{S1.5}$$

At the inlet ($x=0$), $\frac{dC_2^{\infty}}{dx}|_{x=0}\approx 0$ and $C_2^{\infty}(x=0)=C_2^0$, which leads to,

$$J_C \approx 2\bar{u}C_2^0 . \qquad \text{S1.6}$$

Substituting Eq. S1.6 to Eq. S1.5 yields that,

$$-D_2\frac{dC_2^{\infty}}{dx}+(C_2^{\infty}-C_2^0)\bar{u}\approx 0 . \qquad \text{S1.7}$$

Therefore, $C_2^{\infty}(x)\approx C_2^0+Ae^{\frac{\bar{u}}{D_2}x}$, where A is a constant.

We define the downstream anion concentration (after depletion) as C_2^d. At the nanochannel arrays ($x=L/2$), we have $C_2^{\infty}(x=\frac{L}{2})=C_2^d$, which leads to,

$$C_2^{\infty}(x)\approx\left(1-\Psi e^{\mathrm{Pe}\cdot\frac{x}{L/2}}\right)\cdot C_2^0, (x<L/2) \qquad \text{S1.8}$$

where $\Psi=(1-\frac{C_2^d}{C_2^0})e^{-\mathrm{Pe}}$ and $\mathrm{Pe}=\frac{\bar{u}(L/2)}{D_2}$, with Pe being the Péclet number of the system.

Substituting Eq. S1.6 and Eq. S1.8 to Eq. S1.4 yields that,

$$E(x)\approx\frac{\bar{u}}{\mu_2}\cdot\frac{1}{1-\Psi e^{\mathrm{Pe}\cdot\frac{x}{L/2}}} . \qquad \text{S1.9}$$

Up to this point, the distributions of buffer ions and the electric field have been solved.

Next, by substituting Eq. S1.9 to Eq. S1.3 and applying the boundary condition $C_3^{\infty}(x=0)=C_3^0$, one can obtain the distribution of the analyte concentration along the x-axis as,

$$C_3^{\infty}(x)\approx\left(\frac{1-\Psi e^{\mathrm{Pe}\cdot\frac{x}{L/2}}}{1-\Psi}\right)\cdot e^{(1-\frac{b}{a})\cdot\mathrm{Pe}\frac{x}{L/2}}\cdot C_3^0 . \qquad \text{S1.10}$$

At the concentration peak (C_{EK}^{∞}), $\frac{dC_3^{\infty}(x)}{dx}=0$, from which one can obtain that,

$$C_{EK}^{\infty}\approx\left[\frac{1}{\Psi}(1-\frac{\mu_3}{\mu_2})\right]^{\frac{D_2}{D_3}(1-\frac{\mu_3}{\mu_2})}\left(\frac{1}{1-\Psi}\frac{\mu_3}{\mu_2}\right)^{\frac{D_2\mu_3}{D_3\mu_2}}C_3^0 . \qquad \text{S1.11}$$

Under conditions of $C_2^0\gg C_2^d$ (due to the ion depletion effect) and $e^{\mathrm{Pe}}\gg 1$ (e^{Pe}= 609 and 35614 for V_{cn}=2V_T and V_{cn}=15V_T, respectively.), Eq. S1.11 can be simplified to,

$$C_{EK}^{\infty}\approx\left(1-\frac{\mu_3}{\mu_2}\right)^{\frac{D_2}{D_3}(1-\frac{\mu_3}{\mu_2})}\cdot\left(\frac{\mu_3}{\mu_2}\right)^{\frac{D_2\mu_3}{D_3\mu_2}}\cdot\left(e^{\mathrm{Pe}}\right)^{\frac{D_2}{D_3}(1-\frac{\mu_3}{\mu_2})}\cdot C_3^0 . \qquad \text{S1.12}$$

Defining $a = \frac{D_2}{D_3}$, $b = \frac{Z_3}{Z_2}$, $\frac{b}{a} = \frac{\mu_3}{\mu_2}$, Eq. S1.12 can be re-written as,

$$C_{EK}^{\infty} \approx a^{-a} b^{b} (a-b)^{(a-b)} \cdot e^{(a-b)\cdot \mathrm{Pe}} \cdot C_3^0 \quad \text{S1.13}$$

Section 2. Derivation of the EN limit

At the steady state, the fluxes of all charged species are constant along the *x*-axis ($x<L/2$). Considering the inlet and the concentration plateau, one can have $J_1^\infty(\text{in}) = J_1^\infty(\text{p})$, $J_2^\infty(\text{in}) = J_2^\infty(\text{p}) \approx 0$, $J_3^\infty(\text{in}) = J_3^\infty(\text{p}) \approx 0$, where "in" denotes the inlet, and "p" denotes the concentration plateau. These equations can be expanded to,

$$-D_1\frac{dC_1^\infty(\text{in})}{dx} + (\overline{u} + \mu_1 E_{\text{in}})C_1^\infty(\text{in}) = -D_1\frac{dC_1^\infty(\text{p})}{dx} + (\overline{u} + \mu_1 E_{\text{p}})C_1^\infty(\text{p}), \quad \text{S2.1}$$

$$-D_2\frac{dC_2^\infty(\text{in})}{dx} + (\overline{u} - \mu_2 E_{\text{in}})C_2^\infty(\text{in}) = -D_2\frac{dC_2^\infty(\text{p})}{dx} + (\overline{u} - \mu_2 E_{\text{p}})C_2^\infty(\text{p}) \approx 0, \quad \text{S2.2}$$

$$-D_3\frac{dC_3^\infty(\text{in})}{dx} + (\overline{u} - \mu_3 E_{\text{in}})C_3^\infty(\text{in}) = -D_3\frac{dC_3^\infty(\text{p})}{dx} + (\overline{u} - \mu_3 E_{\text{p}})C_3^\infty(\text{p}) \approx 0. \quad \text{S2.3}$$

At the inlet, the concentrations of all charged species equal the initial concentration, and the concentration gradients can be considered zero. At the concentration plateau, the concentration gradients of all charged species are zero. Therefore, $C_i^\infty(\text{in}) = C_i^0$, $\frac{dC_i^\infty(\text{in})}{dx} = 0$, $\frac{dC_i^\infty(\text{p})}{dx} = 0$, i=1, 2, 3. Eqs. S2.1-S2.3 can be reduced to,

$$(\overline{u} + \mu_1 E_{\text{in}})C_1^0 = (\overline{u} + \mu_1 E_{\text{p}})C_1^\infty(\text{p}), \quad \text{S2.4}$$

$$(\overline{u} - \mu_2 E_{\text{in}})C_2^0 = (\overline{u} - \mu_2 E_{\text{p}})C_2^\infty(\text{p}) \approx 0, \quad \text{S2.5}$$

$$(\overline{u} - \mu_3 E_{\text{in}})C_3^0 = (\overline{u} - \mu_3 E_{\text{p}})C_3^\infty(\text{p}) \approx 0. \quad \text{S2.6}$$

In Eq. S2.5, the total flux is zero, and C_2^0 is much greater than zero, one can have,

$$\overline{u} \approx \mu_2 E_{\text{in}}. \quad \text{S2.7}$$

In Eq. S2.6, the total flux is zero, and $C_3^\infty(\text{p})$ is much greater than zero, one can have,

$$\overline{u} \approx \mu_3 E_{\text{p}}. \quad \text{S2.8}$$

From Eq. S2.7 and Eq. S2.8, one can have,

$$E_{\text{p}} \approx \frac{\mu_2}{\mu_3} E_{\text{in}}. \quad \text{S2.9}$$

Substituting Eq. S2.7 and Eq. S2.9 to Eq. S2.4 yields that,

$$C_1^\infty(\text{p}) \approx \frac{\mu_1/\mu_2 + 1}{\mu_1/\mu_3 + 1} C_1^0. \quad \text{S2.10}$$

At the concentration plateau, $C_2^\infty(\text{p}) \approx 0$, so the electroneutrality condition requires that,

$$Z_1 C_1^\infty(\text{p}) + Z_3 C_3^\infty(\text{p}) \approx 0. \quad \text{S2.11}$$

Combining Eq. S2.10 and Eq. S2.11 gives that,

$$C_{EN}^\infty = C_3^\infty(\text{p}) \approx -\frac{Z_1}{Z_3} \cdot \frac{\mu_1/\mu_2 + 1}{\mu_1/\mu_3 + 1} \cdot C_1^0. \quad \text{S2.12}$$

Note that this equation is generally applicable to arbitrary binary electrolytes. For symmetric electrolytes, Eq. S2.12 can be reduced to,

$$C_{EN}^{\infty} \approx \frac{2}{a+b} \cdot C_1^0 \,. \qquad \text{S2.13}$$

Section 3. The relation between $\bar{u}$ and V_{cn}

The velocity profile of the system is shown in Fig. S3-1. The action of a tangential electric field upon the induced space charges near the nanochannel arrays induces a non-equilibrium electroosmotic flow, which is named the electroosmosis of the second kind (EOF2) by Dukhin *et al.*[1] This electroosmotic slip is much faster (>10x) than the primary electroosmosis (EOF1) in the bulk channel. Consequently, a pair of vortices is generated near the nanochannel arrays to satisfy the incompressibility of fluid. At the same time, a pressure-driven flow is induced in the bulk channel that speeds up the net fluid velocity ($\bar{u}$), as indicated by the parabolic flow profiles at higher V_{cn}'s.

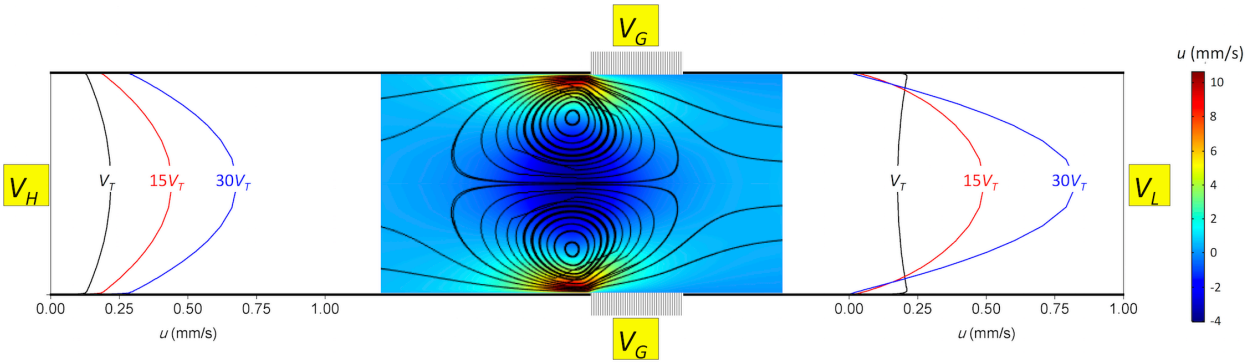

Fig. S3-1 Fluid velocity profiles in the central microchannel. The electrical configuration is V_{HL}=20V_T, with V_{cn} labeled on each curve. The color map represent the x-direction velocity (u) at V_{cn}=20V_T.

Theoretical modeling of the fluid flow of the system is challenging, as it involves the coupling of EOF1 and EOF2. Rubinstein *et al.*[2-5] and Kim *et al.* [6] studied the symmetric case of the system (V_H=V_L), in which there is no net tangential fluid flow ($\bar{u}=0$). According to their studies, the EOF2 slip velocity (u_{s2}) near the nanochannel surfaces is proportional to the square or cube of V_{cn}, depending on the magnitude of the electric field applied. This nonlinear dependence is observed in our model by setting V_H=V_L, as shown in Fig. S3-2.

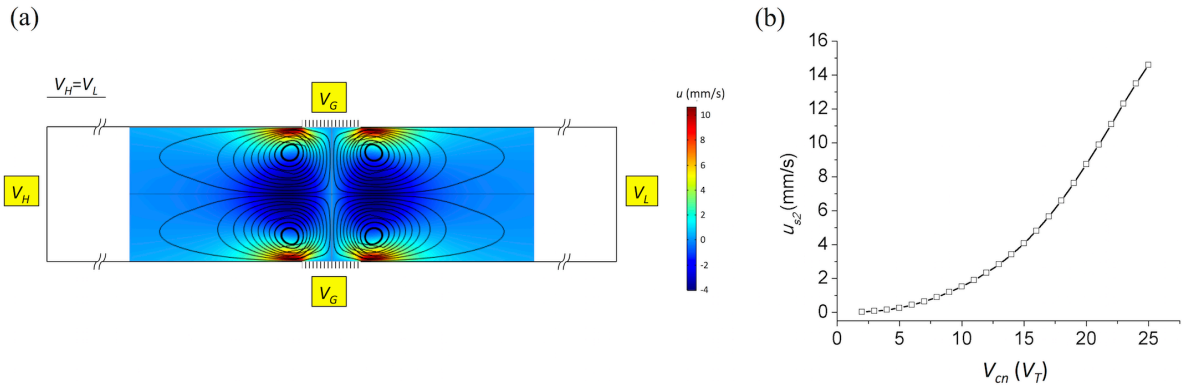

Fig. S3-2. (a) Velocity streamlines and velocity magnitude in a symmetric system. The color map represent the x-direction velocity (u) at V_{cn}=21V_T. (b) The EOF2 slip velocity (u_{s2}) in the vicinity of the nanochannel arrays (x=59 μm).

However, when the symmetry is broken ($V_{HL}=V_H-V_L>0$), EOF2 contributes to the net tangential fluid flow. Fig. S3-3(a) shows the velocity profiles along the cross-section of the channel in the vicinity of the nanochannel arrays (x=59 μm) at different V_{cn}'s. We take the maximum velocity as the EOF2 slip velocity (u_{s2}). As shown in Fig. S3-3(b), u_{s2} is proportional to V_{cn}, which is clear departure from the scaling relation in the symmetric scenario. The detailed mechanism calls for further theoretical studies.

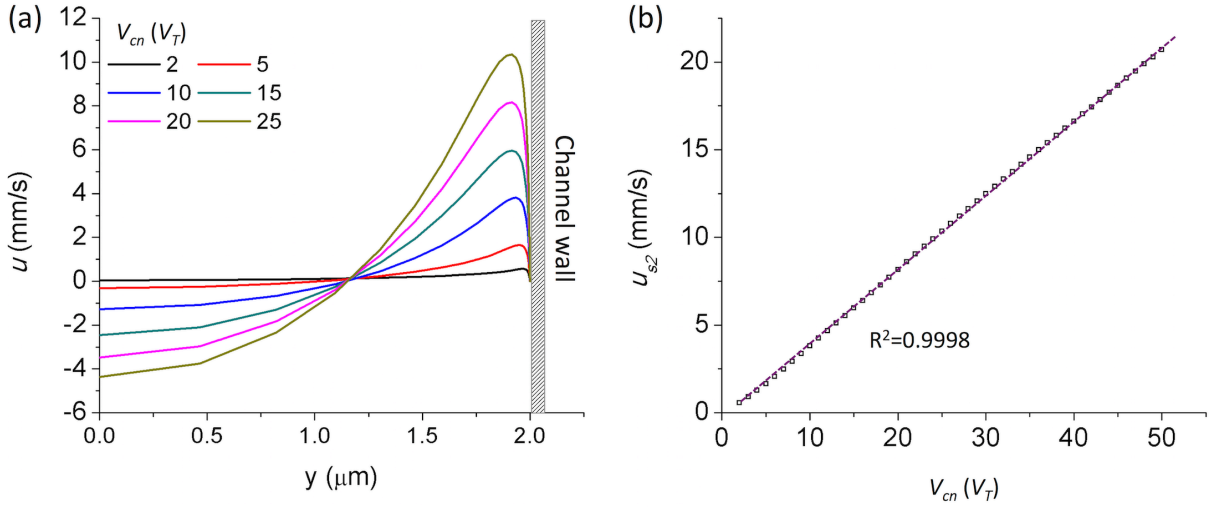

Fig. S3-3. (a) The x-direction velocity (u) profiles along the cross-section of the channel in the vicinity of the nanochannel arrays (x=59 μm) at different V_{cn}'s at V_{HL}=15V_T. (b) Dependence of the EOF2 slip velocity (u_{s2}) on V_{cn} at V_{HL}=15V_T.

Fig. S3-4 shows the dependence of $\bar{u}$ on V_{cn} and V_{HL}. When V_{cn} is relatively low compared to V_{HL}, the system is dominated by the tangential electric field set up by V_{HL}. In this regime, $\bar{u}$ is mainly determined by EOF1, because EOF2 is relatively low due to the weak ion depletion effect. Consequently, $\bar{u}$ increases approximately linearly with V_{cn} at a small slope, as lowering V_n also increases the upstream tangential electric field that drives EOF1. As V_{cn} further increases, the system becomes dominated by the electric field set up by V_H and V_n. In this regime, $\bar{u}$ is mainly determined by EOF2. Because EOF2 is linear with V_{cn} as aforementioned and EOF2 is much faster than EOF1, $\bar{u}$ increases linearly with V_{cn} with a large slope. Lastly, the higher V_{HL} is, the higher V_{cn} is needed to enter the EOF2-dominated regime.

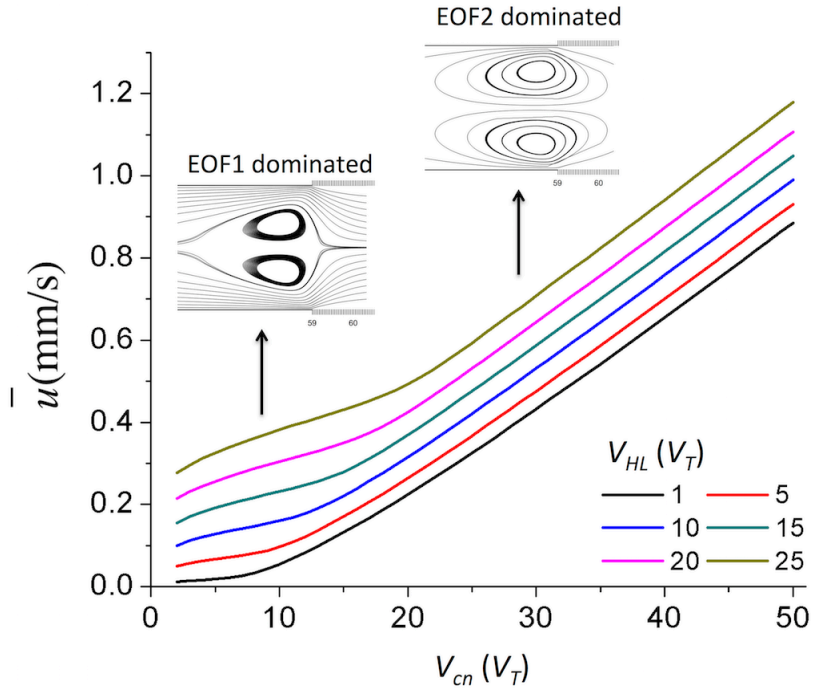

Fig. S3-4. Dependence of the net fluid velocity $\bar{u}$ on V_{HL} and V_{cn}. When V_{cn} is small, $\bar{u}$ is dominated by EOF1, which is approximately linear with V_{cn}. When V_{cn} is large, $\bar{u}$ is dominated by EOF2, which is linear with V_{cn} with a higher slope than that of the EOF1-dominated regime.

Section 4. Effect of the electrophoretic mobility of buffer ions

We will only discuss symmetric electrolytes, where the electrophoretic mobility of the cation and anion equals ($\mu_1 = \mu_2$). We will simply use μ_2 to refer to the electrophoretic mobility of the buffer ions.

The high electrophoretic mobility of buffer ions accelerates the transport of cations through the ion depletion zone and the nanochannels, and the repulsion of anions from the ion depletion zone, thereby forming ion depletion zones with lower ion concentrations, as shown in Fig. S4-1(a). Consequently, thicker extended space charge layers are formed in the ion depletion zone in buffers of higher ion mobility, as indicated by the color maps in Fig. S4-1(b). According to the Poisson equation, more abrupt changes of the electric field exist in the ion depletion zone at higher ion mobility, which leads to stronger electric fields, as indicated by the arrows in Fig. S4-1(b). As a result, the non-equilibrium EOF in the ion depletion zone is accelerated and the trapping of the analyte is enhanced, leading to higher CFs.

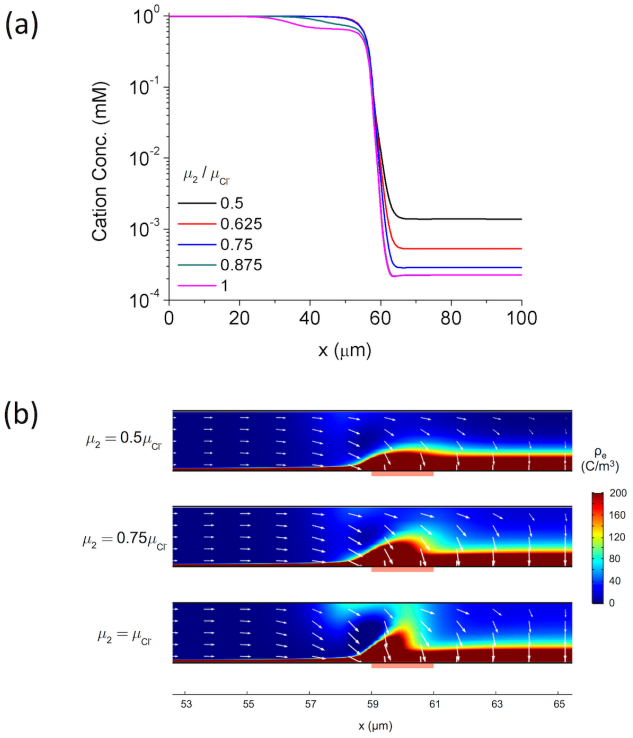

Fig. S4-1. Effect of the electrophoretic mobility of buffer ions. (a) Cation concentration profiles at different ion mobility. (b) The space charge density (color map) and the electric field (arrows plotted in natural logarithm-scale at different ion mobility.

Section 5. Meshing issues

We adopted non-uniform distributed meshes to discretize the fluid domain. In the regions near the surface of the channel wall, the intersection of the channel wall and the membrane, as well as the inlet and outlet of the microchannel, the density of the mesh is increased significantly. While in the other regions, relatively coarse meshes are used. For example, to discretize the half width (2 μm) of the microchannel, we use a geometric sequence of 40 elements, with the maximum size being 12000 times larger than the minimum size (0.428 μm near the center of the microchannel and 0.036 nm near the charged surface, respectively). Inside the Electrical Double Layer (~10 nm), there are ~20 layers of exponentially decreased meshes, which provides sufficient details for the physical fields, while total number of meshes is kept small. Similarly, the 1 μm length of the membrane is discretized into 60 elements with the maximum size (in the middle) 30 times larger than the minimum size near the intersection of the membrane and the channel wall. This provides good approximation of the sharp changes of fields like electric potentials, fluid velocities, and ion fluxes at the intersection regions.

To further prove that the simulation is converged and mesh independent, we studied the results of concentration factor, maximum electric field and maximum velocity in the axial direction along the center line of the microchannel using increased mesh densities up to 10 times of our original mesh. The parameters are Z_3=-2, D_3=D_2/4, and V_{cn}=14V_T. From results in the table below, we can find that the differences are negligibly trivial, and there is no clear trend for increasing mesh density. Therefore, we believe that the difference between them is caused largely by random truncation errors, instead of by insufficient mesh densities.

Table S5-1. Comparison between different meshing densities.

Relative mesh density	CF	Max(Ex) (V/cm)	Max (U_x)(mm/s)
1	304.7901175	229.486504707708	0.47307413622658
2	304.7901175	229.486504709585	0.47307413633830
3	304.7901174	229.486504707187	0.47307413631592
4	304.7901175	229.486504708426	0.47307413632509
5	304.7901174	229.486504705944	0.47307413618178
6	304.7901175	229.486504709408	0.47307413632049

7	304.7901176	229.486504710507	0.47307413632845
8	304.7901176	229.486504710479	0.47307413627204
9	304.7901174	229.486504707839	0.47307413632964
10	304.7901175	229.486504707485	0.47307413618932

References:

1. Dukhin, S. S. *Adv. Colloid Interface Sci.* **1991,** 35, 173-196.
2. Rubinstein, I.; Zaltzman, B.; Lerman, I. *Phys. Rev. E* **2005,** 72, (1), 011505.
3. Rubinstein, I.; Zaltzman, B. *Mathematical Models and Methods in Applied Sciences* **2001,** 11, (02), 263-300.
4. Rubinstein, I.; Zaltzman, B. *Phys. Rev. E* **2000,** 62, (2), 2238.
5. Rubinstein, S. M.; Manukyan, G.; Staicu, A.; Rubinstein, I.; Zaltzman, B.; Lammertink, R. G. H.; Mugele, F.; Wessling, M. *Phys. Rev. Lett.* **2008,** 101, (23), 236101.
6. Kim, S. J.; Wang, Y.-C.; Lee, J. H.; Jang, H.; Han, J. *Phys. Rev. Lett.* **2007,** 99, (4), 044501.